Title
PULSED ELECTROSTATIC PROBES AS A DIAGNOSTIC FOR TRANSIENT PLASMAS

Author
Schoenberg, Kurt F.

Publication Date
1978-02-01

Submitted to Review of Scientific Instruments

LBL-7534 c.2
Preprint

PULSED ELECTROSTATIC PROBES AS A DIAGNOSTIC FOR TRANSIENT PLASMAS

Kurt F. Schoenberg

February 1978

Prepared for the U. S. Department of Energy under Contract W-7405-ENG-48

DISCLAIMER

PULSED ELECTROSTATIC PROBES AS A DIAGNOSTIC FOR TRANSIENT PLASMAS*

Kurt F. Schoenberg

Lawrence Berkeley Laboratory, University of California

Berkeley, California 94720

ABSTRACT

A pulsed, electrostatic probe data acquisition system, applicable to transient or noisy plasmas, is presented. The system digitally records a probe characteristic, and its first and second derivatives. The latter are shown to be proportional to the projected electron energy distribution function, and the isotropic electron energy distribution function, respectively. The acquisition system and its experimental accuracy are discussed. Using the Lawrence Berkeley Laboratory 10 ampere neutral beam ion source, several examples demonstrating the systems application to transient plasmas are given.

*Work done under the auspices of the U. S. Department of Energy.

INTRODUCTION

Electrostatic probes have been employed for many years as a useful plasma diagnostic,[1] their main limitations being the experimental accuracy and ease of data acquisition and analysis. Recent developments in both linear and digital electronics have greatly facilitated both the speed and accuracy with which probe data can be obtained. These developments are particularly useful in transient or noisy plasmas where high speed data acquisition is imperative. This paper presents a pulsed electrostatic probe data acquisition system, used to study the electron-ion density and electron energy distribution function in the Lawrence Berkeley Laboratory 10 ampere neutral beam ion source.

THEORY OF MEASUREMENT

The LBL ion source operates in a regime where cylindrical or spherical probe operating conditions are adequately described by the collisionless thin sheath approximation.

i.e. $\bar{\lambda} >> r_p >> \lambda_D$ where $\bar{\lambda} \equiv$ Collisional Mean Free Path $\sim \dfrac{18\pi n_e \lambda_D^4}{\ln(12\,\pi n \lambda_D^3)}$

$\lambda_D \equiv$ Electron Debye Length $= \sqrt{kT_e/4\pi n_e e^2}$

$r_p \equiv$ Probe radius

A schematic typical of a probe current-voltage characteristic is shown in Fig. 1. The experimentally important quantities are:

1) Accurate determination of the Plasma Potential V_p.
2) Accurate determination of the Probe Floating Potential V_f.
3) Accurate measurement of the ion-saturation region (A).
4) Accurate measurement of the electron-transition region (B).

For the case where the electron temperature far exceeds the ion temperature, collected ion current density is quite insensitive to ion temperature and is expressed as

$$j_i(V_\phi) = \left(\frac{1}{4} n_i Z_i e \sqrt{\frac{8kT_e}{\pi m_i}}\right) i_+ \, (V_\phi;\, T_e,\, T_i,\, r_p,\, \lambda_D) \qquad (1)$$

where i_+ is an ion current correction factor computed by the theory of Laframboise,[2] and V_ϕ is the probe bias voltage measured with respect to the plasma potential, i.e. $V_\phi = V_p - V$.

The electron current density in the transition region can be expressed in terms of the isotropic electron velocity distribution function $f_e(v)$, as

$$j_e(V_\phi) = n_e e\langle v\rangle(V_\phi) = e \int_{\sqrt{\frac{2eV_\phi}{m_e}}}^{\infty} v^3 f_e(v) \int_{\frac{1}{v}\sqrt{\frac{2eV_\phi}{m_e}}}^{1} \cos\theta\, d(\cos\theta) \int_0^{2\pi} d\phi \qquad (2)$$

Performing the angle integration yields

$$j_e\,(V_\phi) = e\int_{\sqrt{\frac{2eV_\phi}{m_e}}}^{\infty} v^3 f_e(v) \left(1 - \frac{2eV_\phi}{m_e v^2}\right) dv \qquad (3)$$

Considering that electron current density is experimentally measured as a function of bias potential, a more convenient description of $j_e(V_\phi)$ is obtained by expressing it as a function of $f_e(\varepsilon)$, the isotropic electron energy distribution function. Defining $f_e(\varepsilon)$ as

$$f_e(\varepsilon) = \int_0^{\infty} f_e(v)\,\delta(\varepsilon - \tfrac{1}{2} m_e v^2)\,dv \qquad (4)$$

equation (3) becomes

$$j_e(V_\phi) = \frac{2\pi e}{m_e^2} \int_{eV_\phi}^{\infty} \varepsilon\, f_e(\varepsilon) \left(1 - \frac{eV_\phi}{\varepsilon}\right) d\varepsilon \qquad (5)$$

For the special case of a Maxwellian Plasma,

$$f_e(\varepsilon) = n_e \left(\frac{m_e}{2\pi kT_e}\right)^{3/2} e^{-\varepsilon/kT_e} \qquad (6)$$

which when substituted into equation (5), yields the familiar result

$$j_e(V_\phi) = \frac{1}{4} n_e e \sqrt{\frac{8kT_e}{\pi m_e}}\ e^{-eV_\phi/kT_e} \tag{7}$$

where the electron temperature is given by the inverse slope of $\ln j_e(V_\phi)$ vs V_ϕ. For the general case where $f_e(\varepsilon)$ deviates from a Maxwellian, the electron current density will behave according to equation (5). The fact that $j_e(V_\phi)$ is related to $f_e(\varepsilon)$ through an integral equation, coupled with experimental measurement uncertainties, makes it quite insensitive to all but gross distribution function structure. Finer grained resolution is possible by performing the first and second derivatives of $j_e(V_\phi)$. Taking the second derivative with respect to bias voltage of equation (5) yields

$$\frac{d^2 j_e(V_\phi)}{dV_\phi^{\ 2}} = \frac{d}{dV_\phi}\left(\frac{2\pi e}{m_e^{\ 2}} \int_{eV_\phi}^{\infty} \frac{\partial}{\partial V_\phi}\, \varepsilon f_e(\varepsilon)\left(1 - \frac{eV_\phi}{\varepsilon}\right) d\varepsilon\right) = \frac{2\pi e^3}{m_e^{\ 2}} f_e(V_\phi) \tag{8}$$

Hence,

$$f_e(\varepsilon) = \frac{m_e^{\ 2}}{2\pi e^3} \left.\frac{d^2 j_e(V_\phi)}{dV_\phi^{\ 2}}\right|_{eV_\phi = \varepsilon} \tag{9}$$

which relates the electron energy distribution function to the second derivative of the electron probe current density.[3]

The above treatment required $f_e(\varepsilon)$ to be isotropic. A generalization for non-isotropic distribution functions is possible by defining $f_e(u,\hat{n})$, the projected electron velocity distribution function in the spatial direction $\hat{n}$, as

$$f_e(u,\hat{n}) = \int_{\text{all } \vec{v}} d\vec{v}\ f_e(\vec{v})\,\delta(\hat{n}\cdot\vec{v} - u) \tag{10}$$

where $f_e(\vec{v})$ is the general electron velocity distribution function. In terms of $f_e(u, \hat{n})$, equation (2) reduces to

$$j_e(V_\phi) = e \int_{\sqrt{\frac{2eV_\phi}{m_e}}}^{\infty} f_e(u, \hat{n})\, u\, du \qquad (11)$$

where $\hat{n}$ now refers to the spatial direction normal to the probe surface. Again, defining $f_e(\varepsilon, \hat{n})$, the projected electron energy distribution function as

$$f_e(\varepsilon, \hat{n}) = \int_{o}^{\infty} f_e(u, \hat{n})\,\delta(\varepsilon - \frac{1}{2} mu^2)\, du \qquad (12)$$

equation (11) becomes

$$j_e(V_\phi) = \frac{e}{m_e} \int_{eV_\phi}^{\infty} f_e(\varepsilon, \hat{n})\, d\varepsilon \qquad (13)$$

Performing the first derivative with respect to bias voltage yields

$$\frac{dj_e(V_\phi)}{dV_\phi} = -\frac{e^2}{m_e} f_e(V_\phi, \hat{n}) \qquad (14)$$

or

$$f_e(\varepsilon, \hat{n}) = -\frac{m_e}{e^2} \frac{dj_e(V_\phi)}{dV_\phi}\Bigg|_{eV_\phi = \varepsilon} \qquad (15)$$

When used with a judiciously designed plane or wall probe, equation (15) affords a convenient method of measuring the projected distribution function in any spatial direction.

EXPERIMENTAL APPARATUS

1. Plasma Source

Figure 2 illustrates a cross-sectional schematic of the LBL 10-ampere neutral beam ion source.[4] The source produces a plasma via a diffuse, low pressure, high current electrical discharge. The arc ionization is produced by primary electrons originating at the thermionic cathode (filament ring), and energized by their passage through the cathode-plasma sheath. The arc discharge occurs between the filament ring, consisting of 26 hairpin tungsten filaments connected in parallel, and the anode ring. A pulse line composed of iron core inductors and electrolytic capacitors, supplies arc power for up to 100 msec. Arc operating conditions range from 10 to 60 kilowatts yielding electron-ion densities of $1.0 \cdot 10^{12}/cm^3$ to $8.0 \cdot 10^{12}/cm^3$ and bulk electron temperatures of 3 to 5 eV. All source walls electrically float at potentials such that the net random current due to electron and ion bombardment is nulled. Access to the plasma is via three radial probe ports at the source midplane, and one section of axially symmetric floating wall which is used as an extended wall probe.

2. Probe Driver/Detection Circuit

The motivation for a pulsed detection circuit, in addition to the plasma's transient nature, is readily apparent from its noise spectrum (Fig. 3). The large noise increase below 1 kHz is presumably due to power supply effects. Data acquisition in a time less than 1 ms is necessary to minimize this noise influence.

Figure 4 schematically illustrates the probe driver/detection circuit. An initial pulse, obtained from the source logic, operates the timing of various source inputs. (e.g. application of arc power, filament power, gas injection, etc.) The pulse is also applied to a variable delay gate (enabling data acquisition at any subsequent moment during source operation), amplified, and then used to trigger the probe driver and data recording system. The probe driver initially applies a large positive bias to the probe to insure a clean collection surface, followed by a linearly decreasing voltage ramp which sweeps the probe bias over its entire operating range. Sweep speeds of .1 v/μsec to 1 v/μsec over a total range of 100 volts are typical. The probe current is differentially detected across a standard resistance and then processed by the differentiation network, which outputs the probe current and its first and second derivatives. These signals are digitally recorded by a Nicolet transient digitizer, which simultaneously samples the processed current signal and its corresponding bias voltage. The stored data is accessible both graphically and as a digitized data set of points. This output format presently allows rapid data analysis with minimal measurement error. The system also has the option of a direct computer data link, allowing for real time data analysis.

The differentiation network (Fig. 5) consists of a series of ganged stages, each stage tailored to a particular frequency response which minimizes overall network noise and instability, while maintaining differentiation accuracy over a 100 kHz bandwidth. All stages utilize compensated AD 507 wideband, low noise operational amplifiers, which have proven quite cost effective. Components for the differentiation stages (Fig. 6) were chosen to insure a 6 dB/octave gain increase over a 100 kHz bandwidth and stability over all operating conditions. Buffer stages are low pass Butterworth filters with flat pass bands from 0-100 kHz.

ACCURACY ANALYSIS

The accuracy of the data acquisition process is dependent on both the response characteristic of the probe driver circuit, and the acquisition accuracy of the probe current detection network.

A circuit equivalent model of the probe/driver is illustrated in Fig. 7. A discrete circuit model should remain a reasonable approximation for response times slow compared to an ion plasma period. The temporal response of the circuit model is roughly

$$\tau_{system} = \frac{R_D R_S \; (C_D + C_S)}{(R_D + R_S)} \tag{16}$$

where $C_D(R_D)$ are the effective driver circuit capacitance (resistance) and $C_S(R_S)$ are the effective probe-plasma sheath capacitance (resistance) respectively. For realistic experimental systems, $C_S << C_D$ [5] and R_D can usually be made much smaller than R_S thru judicial driver circuit and probe design. Therefore, the probe driver electronics completely determines the temporal response of the system. The measured frequency response of the driver section depicted in Fig. 7, was linear over a 100-kHz bandwidth, with a loaded slew rate of 10 V/μsec.

Since temporal variations in the probe current signal are related to voltage variations via a linear bias voltage ramp ($V_\phi \propto t$), differentiation network accuracy is also dependent on temporal response. The spectral density of the probe current density j(t), is given by its Fourier Transform

$$J(\omega) = \int_{-\infty}^{\infty} j(t) \; e^{-i\omega t} dt \tag{17}$$

Given $D(\omega)$, the network response function of the detection system, the detected current density is

$$j_{DET}(t) = \frac{1}{2\pi}\int_{-\infty}^{\infty} D(\omega)\ J(\omega)\ e^{i\omega t} d\omega = \int_{-\infty}^{t} d(t-\tau) i(\tau) d\tau \qquad (18)$$

where $d(t-\tau)$, the Network Transfer Function, is given by

$$d(t-\tau) = \frac{1}{2\pi}\int_{-\infty}^{\infty} D(\omega)\ e^{i\omega(t-\tau)} d\omega \qquad (19)$$

A rather exact form of $D(\omega)$ is obtainable from frequency response measurements for each of the network functions of interest, although an analytic solution of equation (19) is practically unobtainable. Numerical solutions of equations (19) and (18) are possible, albeit somewhat tedious. For estimation purposes, a reasonable solution of equation (19) is obtainable by noting that since all network functions perform effectively over a 100-kHz bandwidth, the analysis of network accuracy reduces to finding the effect of a finite bandwidth response on the detected signal. This response can be modeled by the step function

$$\begin{aligned} D(\omega) &= 1 \qquad 0 \leq |\omega| \leq \omega_c \\ &= 0 \qquad |\omega| > \omega_c \end{aligned} \qquad (20)$$

where ω_c is the angular high frequency cut-off. Substituting in equation (19) yields

$$d(t-\tau) = \frac{\omega_c}{\pi} \text{Sinc}[\omega_c(t-\tau)] \qquad (21)$$

From equation (18), the approximate detected signal is therefore

$$\begin{bmatrix} j(t) \\ j'(t) \\ j''(t) \end{bmatrix}_{DET} \simeq \frac{\omega_c}{\pi} \int_{-\infty}^{t} \text{Sinc}[\omega_c(t-\tau)] \begin{bmatrix} j(\tau) \\ j'(\tau) \\ j''(\tau) \end{bmatrix} d\tau \qquad (22)$$

Figure 8 illustrates the Sinc transfer function, with a temporal resolution of roughly $1/2f_c$. For f_c = 100 kHz, the temporal resolution is approximately 5 μsec, which corresponds to a voltage resolution of ½ volt for a sweep speed of .1 V/μsec.

ION CURRENT EFFECTS

Equations (9) and (15) relate the electron distribution function to derivatives of the electron probe current. However, since the differentiation network operates on the total probe current, it is necessary to examine the effect of ion current on distribution function measurements.

Under the operating conditions encountered in the Berkeley source, an analytic expression for the ion current as a function of probe bias does not exist. This is primarily due to electron thermal effects which, for an ion attracting probe, allow an electric potential of approximately kT_e to exist in the quasi-neutral plasma region exterior to the plasma-probe sheath. Thus, for the case where $T_i < T_e$, ion probe current is quite insensitive to ion temperature and mainly depends on the complex relation between plasma sheath growth and probe operating parameters. To obtain the exact form of this relation requires a numerical solution of the equations which govern the behavior of ion attracting probes in a collisionless plasma.

One numerical calculation which is particularly well suited for the plasma conditions prevalent in the Berkeley source, is given by Laframboise.[2]

Recall that within the Laframboise theory, ion probe current density as a function of probe bias is described by equation (1). Several approximate analytic fits to the numerical results of Laframboise have been made for a wide range of probe-plasma operating conditions.[6] For the Berkeley source, a typical analytic fit to i_+, the ion current correction factor, is given by

$$i_+(V_\phi) = \begin{cases} 0.9\ \chi^{.469} & \text{for } 0 \leq \chi < 2 \quad \text{within } 8\% \\ 1.09\ \chi^{.182} & \text{for } 2 \leq \chi \leq 25 \quad \text{within } 1\% \end{cases} \tag{23}$$

where $\chi = \frac{eV_\phi}{kT_e}$. Defining R as the ratio of $j_i''(V_\phi)$ to $j_e''(V_\phi)$, and utilizing the results of equations (1), (7) and (23) yields

$$R = \frac{\left(\frac{d^2 j_i(V_\phi)}{dV_\phi{}^2}\right)}{\left(\frac{d^2 j_e(V_\phi)}{dV_\phi{}^2}\right)} = \sqrt{\frac{M_e}{M_i}}\,(kT_e)^2 e^\chi \left(\frac{d^2 i_+(V_\phi)}{dV_\phi^2}\right) = \begin{cases} 3.7 \cdot 10^{-3} \left(\frac{e^\chi}{\chi^{1.53}}\right) & \chi < 2 \\ 2.7 \cdot 10^{-3} \left(\frac{e^\chi}{\chi^{1.82}}\right) & \chi \geq 2 \end{cases} \tag{24}$$

Negligible ion effects require $R < 1$, which implies from equation (24) that probe bias remain in the approximate range $.1\ kT_e \leq eV_\phi \leq 10\ kT_e$.

OTHER EFFECTS

A compendium of experimental complications associated with probe measurements is presented in most standard probe references.[3,7] Important effects like probe surface contamination and probe area variation can usually be minimized by careful probe/driver design. However, probe perturbation of the plasma is unavoidable. The degree to which the perturbation effects the probe measurement is a function of probe-plasma operating conditions, and for many systems becomes appreciable only when probe bias approaches the plasma potential, where the collected electron current is large. Regarding the probe current-voltage characteristic, this effect tends to round off the ideally sharp break occuring between the electron transition region and the electron saturation region (Fig. 1). A reasonable approximation of the plasma potential is customarily achieved by linearly extrapolating the two regions in the neighborhood of the break and obtaining their intersection (Fig. 1).

In distribution function measurements, the perturbation's effect appears as a depletion in the number of electrons with energy roughly less than or equal to kT_e. This effect is mitigated by the condition that for most applications, distribution function structure in this energy region is known.

EXPERIMENTAL RESULTS

Figure 9 shows a typical set of experimental data, which consists of a cylindrical probe characteristic and its first and second derivatives. Note that the position of the cursor, indicated by the intersection of the horizontal and vertical fiducial lines, is an artifact of the digital recorder and does not mark the position of a coordinate origin. The digitized coordinates appearing in each of the photographs indicate the plasma potential. Determination of the plasma potential from distribution function measurements agrees, within experimental uncertainty, with the value obtained from the probe characteristic. Analyzed data results are given in Fig. 10.

Figure 10A plots the total electron energy distribution function $F_e(\varepsilon)$, including phase space weighting, i.e. $F_e(\varepsilon) \alpha f_e(\varepsilon)\sqrt{\varepsilon}$. The function is typical of the LBL ion source and consists of cool, thermal electrons which are electrostatically confined by the source wall floating potential, plus a component of high energy, non thermal primaries and degraded primaries. The bulk thermal electrons comprise roughly 95 to 99 percent of the total electron density depending on operating conditions.

Figure 10B is a logarithmic plot of the electron probe current as a function of probe bias voltage. The probe characteristic is analyzed by a computer routine which outputs the bulk electron temperature, electron and ion densities and their respective uncertainties.

ACKNOWLEDGEMENT

My thanks to the Lawrence Berkeley Laboratory Neutral Beam Group for their general support and assistance.

REFERENCES

1. I. Langmuir and H. M. Mott-Smitt, Phys. Rev., 28 (1926), 727.
2. J. G. Laframboise, U.T.I.A.S. R-100 (1966).
3. L. B. Loeb, "Basic Processes of Gaseous Electronics", University of California Press, (1960), 329-373.
4. K. W. Ehlers, W. R. Baker, K. H. Berkner, W. S. Cooper, W. B. Kunkel, R. V. Pyle, and J. W. Stearns, J. Vac, Sci. Technol. 10 (1973), 922-925.
5. B. M. Oliver, R. M. Clements and P. R. Smy, J. Appl. Phys., 44 (1973), 4511.
6. P. M. Chung, L. Talbot and K. H. Touryan, "Electric Probes in Stationary and Flowing Plasmas", Chap. 2, Springer-Verlag, New York, (1975).
7. F. F. Chen, "Electric Probes", in Plasma Diagnostic Techniques (R. H. Huddlestone and S. L. Leonard, eds.), Academic Press, New York, 191-194.

FIGURE CAPTIONS

Figure 1. A typical probe voltage-current characteristic

Figure 2. Schematic cross section of the LBL 10 ampere neutral beam ion source.

Figure 3. Averaged plasma noise power density.

Figure 4. Probe driver-detection schematic.

Figure 5. Differentiation network block diagram.

Figure 6. Differentiation stage with compensation.

Figure 7. Probe/driver equivalent circuit.

Figure 8. $\omega_c/\pi \, \mathrm{Sinc}[\omega_c(t-\tau)]$.

Figure 9A. Cylindrical probe characteristic.

Figure 9B. 1st derivitive of probe characteristic.

Figure 9C. 2nd derivitive of probe characteristic.

Figure 10A. Total electron energy distribution function $F_e(\varepsilon)$.

Figure 10B. Electron probe current characteristic

ANALYSIS ROUTINE OUTPUT RESULTS

Bulk electron temperature:	4.0 ± 0.1 eV
Electron density:	$2.1 \pm 0.4 \cdot 10^{12}/cm^3$
Ion density:	$2.4 \pm 0.2 \cdot 10^{12}/cm^3$

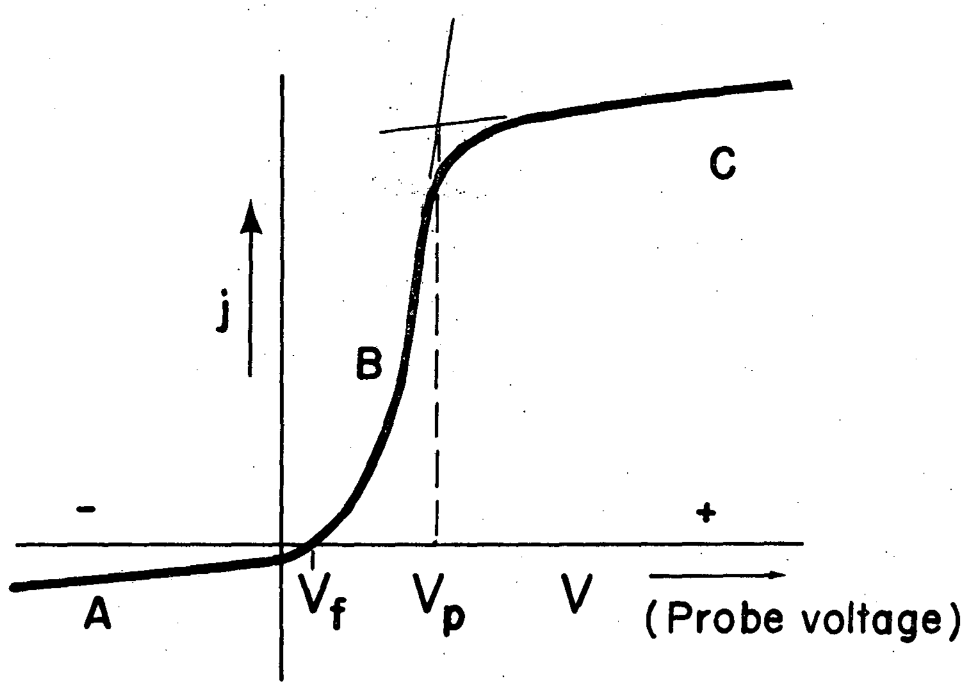

XBL 782-172

Figure 1.

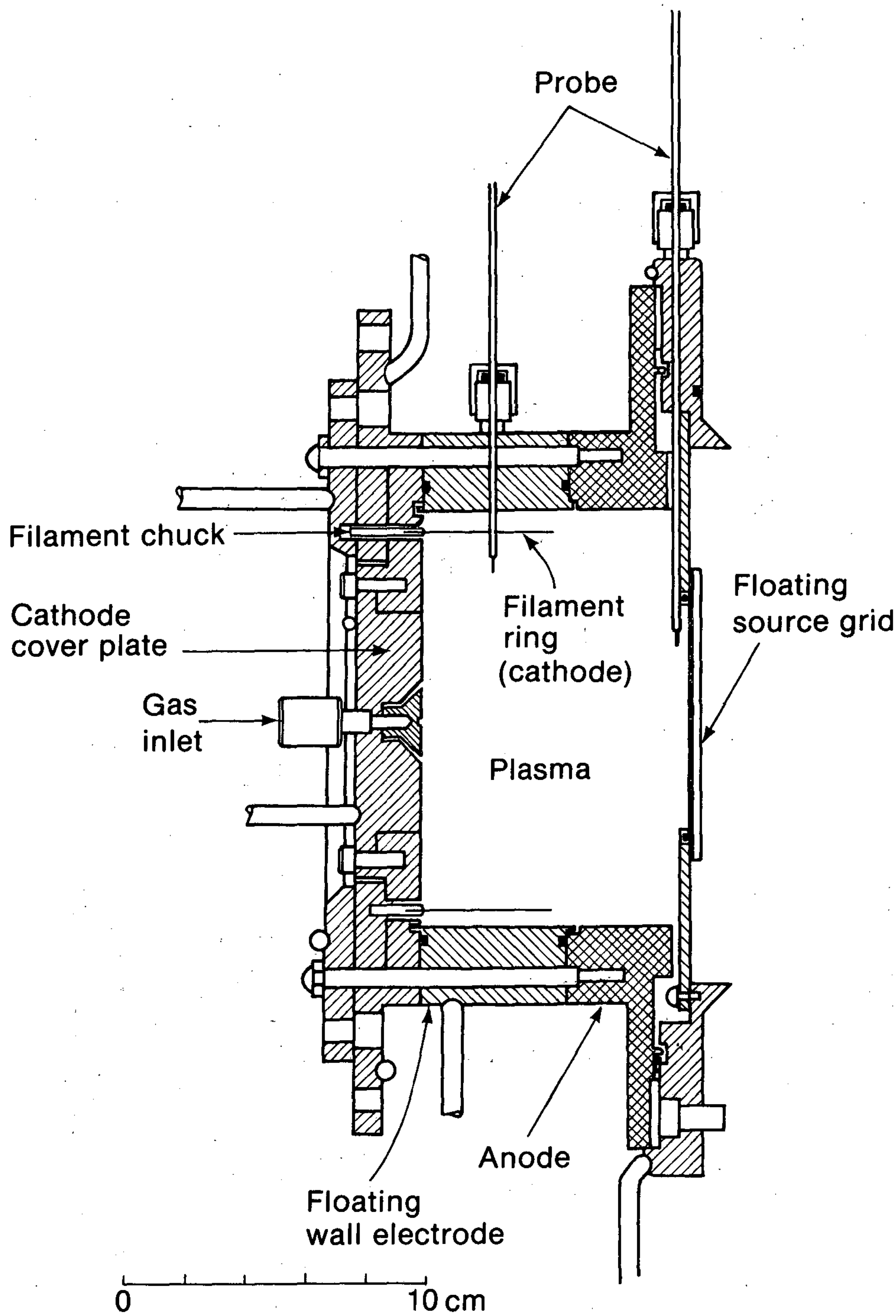

XBL 782-279

Figure 2.

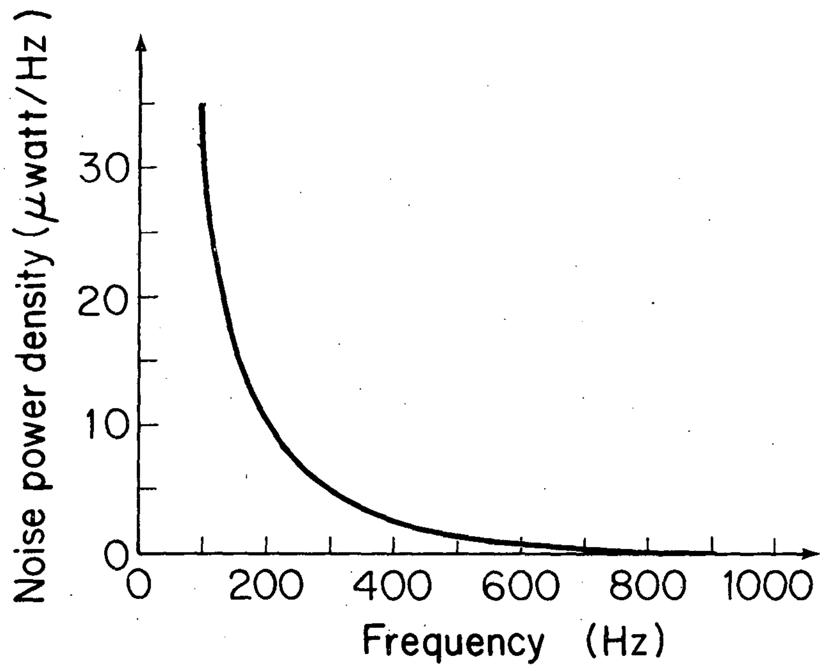

Figure 3.

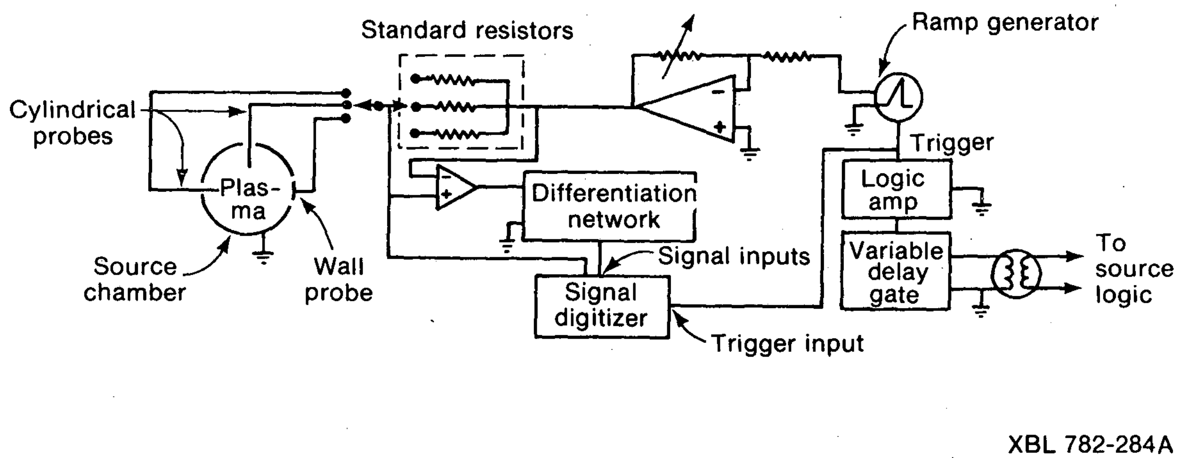

Figure 4.

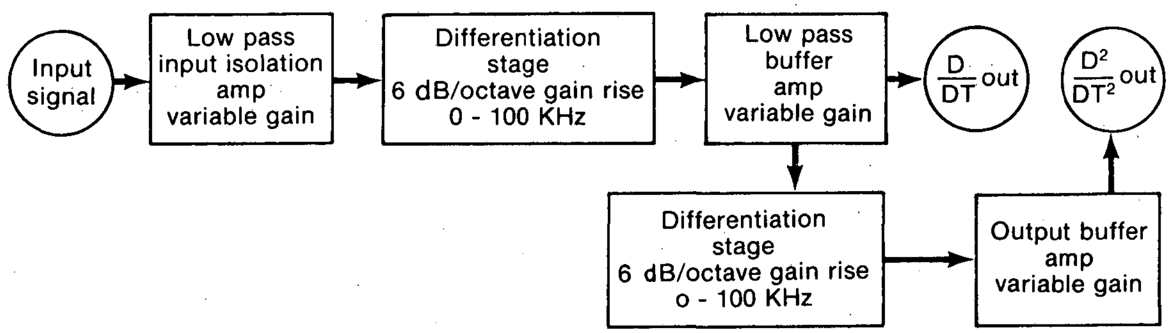

Figure 5.

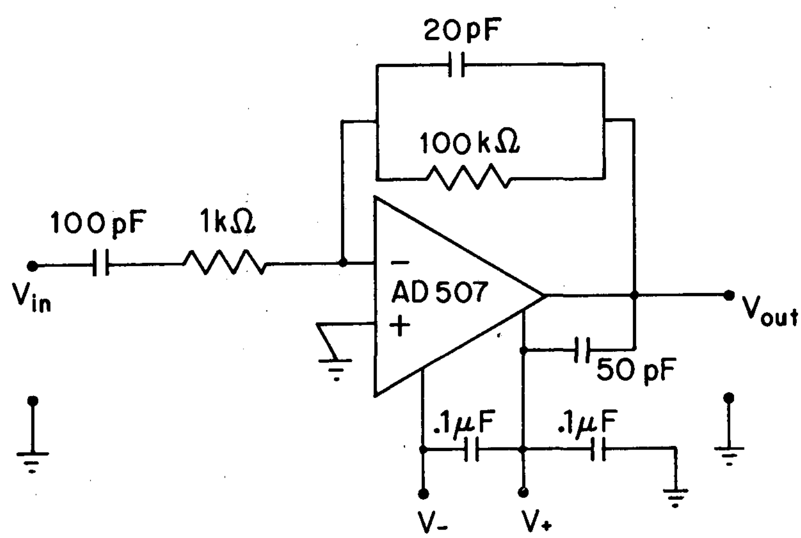

Figure 6.

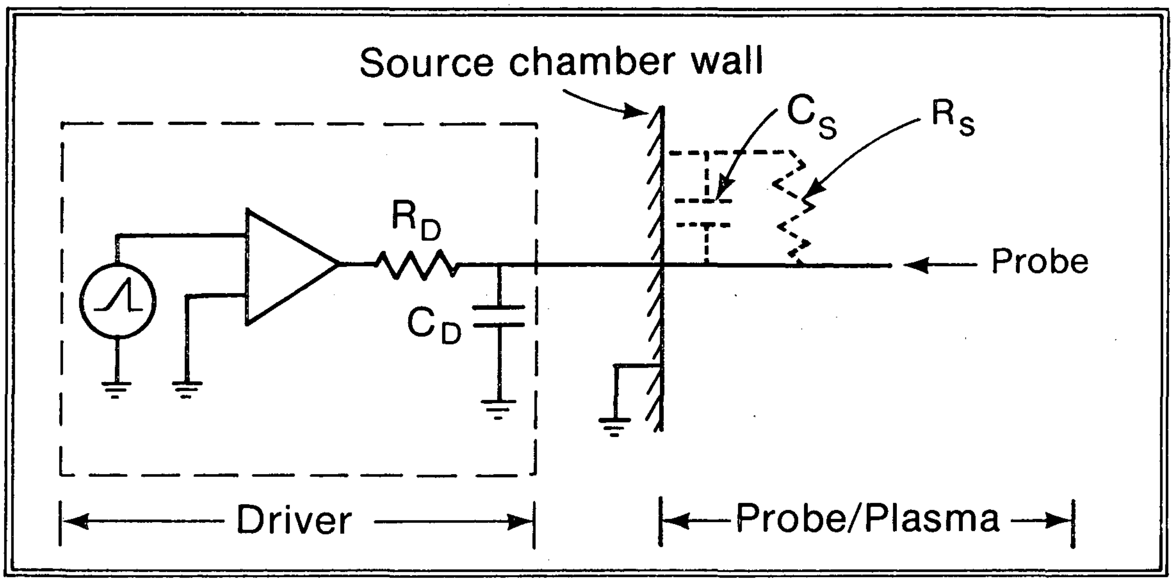

Figure 7.

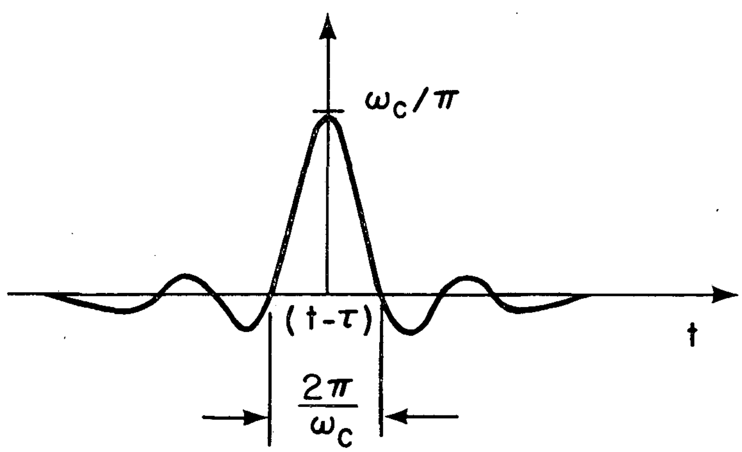

Figure 8.

XBL 782-280A

A)

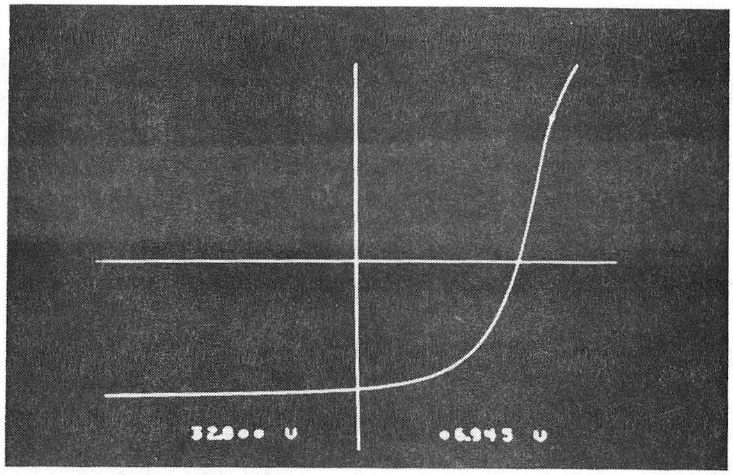

B)

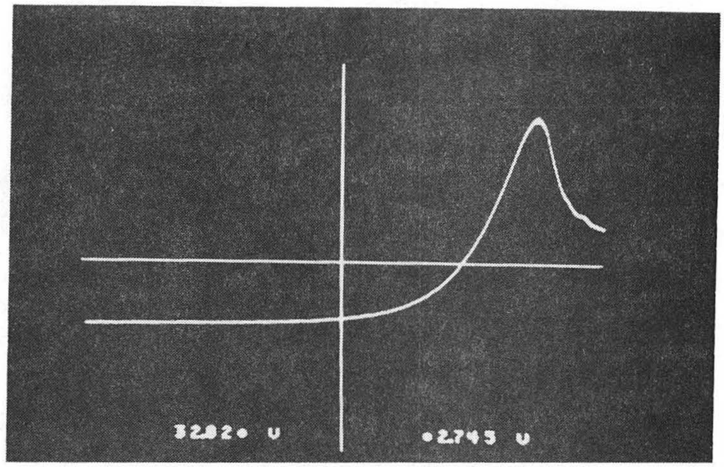

C)

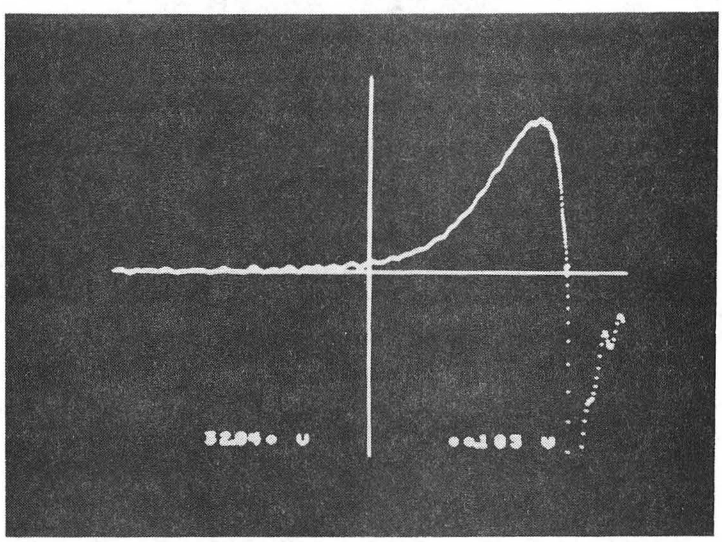

XBB 782-551A

Figure 9.

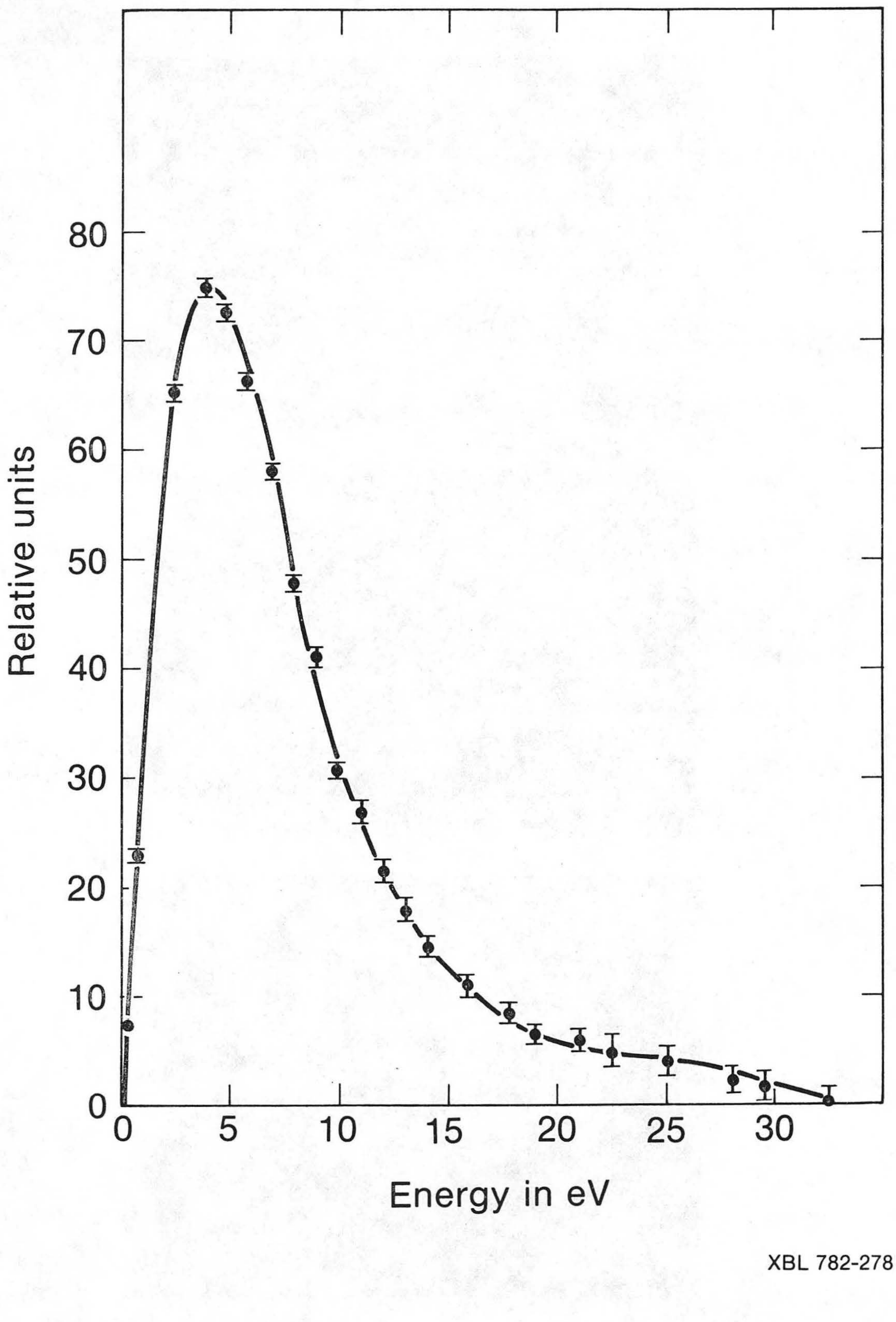
80
70
60
50
40
30
20
10
0
Relative units
0
5
10
15
20
25
30
Energy in eV
XBL 782-278

Figure 10A.

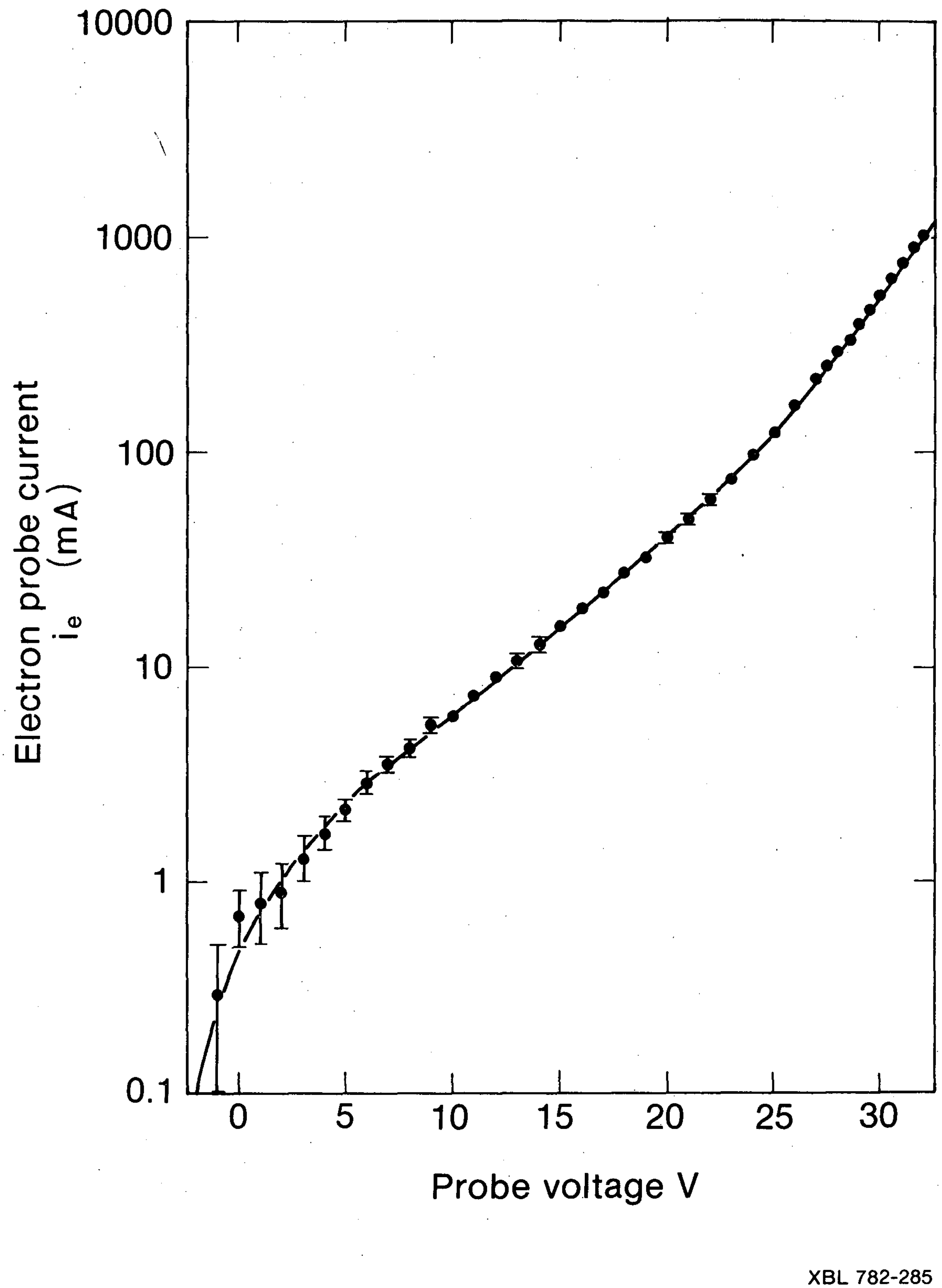
10000
1000
100
10
1
0.1
0
5
10
15
20
25
30
Electron probe current
i_e (mA)
Probe voltage V
XBL 782-285

Figure 10B.

TECHNICAL INFORMATION DEPARTMENT
LAWRENCE BERKELEY LABORATORY
UNIVERSITY OF CALIFORNIA
BERKELEY, CALIFORNIA 94720